Iron Lines from Galactic and Extragalactic X-ray Sources

Kazuo Makishima
Institute of Space and Astronautical Science
4-6-1 Komaba, Meguro-ku, Tokyo, Japan 153.

I. Introduction

Iron is the most abundant heavy element in the universe, believed to be produced in stellar nucleosynthesis. It also has a high fluorescence yield (34%), and its K-line energy (6.4-7 keV) falls right in the middle of the traditional 2-10 keV bandpass of the X-ray astronomy. These facts make iron an ideal "tracer" of the matter distribution and elemental abundance in galactic and extragalactic X-ray sources. However, previous iron-line studies were quite limited due either to a poor energy resolution (proportional counters) or to a low sensitivity (dispersive methods).

This situation has been improved drastically by the gas scintillation proportional counter experiment (GSPC) [KOY84] on board the Tenma satellite [TAN84]. It has a total effective area of 640 cm^2, and a FWHM energy resolution of $\sim$9 % at 6 keV which is at least twice as good as that of conventional proportional counters. It has enabled high-sensitivity, wide-band (1.5-35 keV) spectroscopic studies of many galactic and extragalactic X-ray sources [TAN84,MAK84,INO85a,TAN86]. One of the richest results from the Tenma mission is, in fact, the iron line spectroscopy [INO85a, KOY85]. Table 1 schematically summarizes the merit of the GSPC in comparison with the proportional counters.

Table 1 A schematic comparison of proportional counters (PC) and gas scintillation proportional counters (GSPC) in cosmic iron-line spectroscopy.

	Strong line		Weak line	
	PC	GSPC	PC	GSPC
line detection	YES	YES	NO	YES
line center energy	MAYBE	YES	NO	YES
line intensity	NO	YES	NO	MAYBE
intrinsic line width	NO	MAYBE	NO	NO

For later use, we present in Fig.1 the iron K-edge energy and the iron K-alpha emission line energy as a function of the ionization degree. Also in Fig.2 we present the relative ionization population of iron.

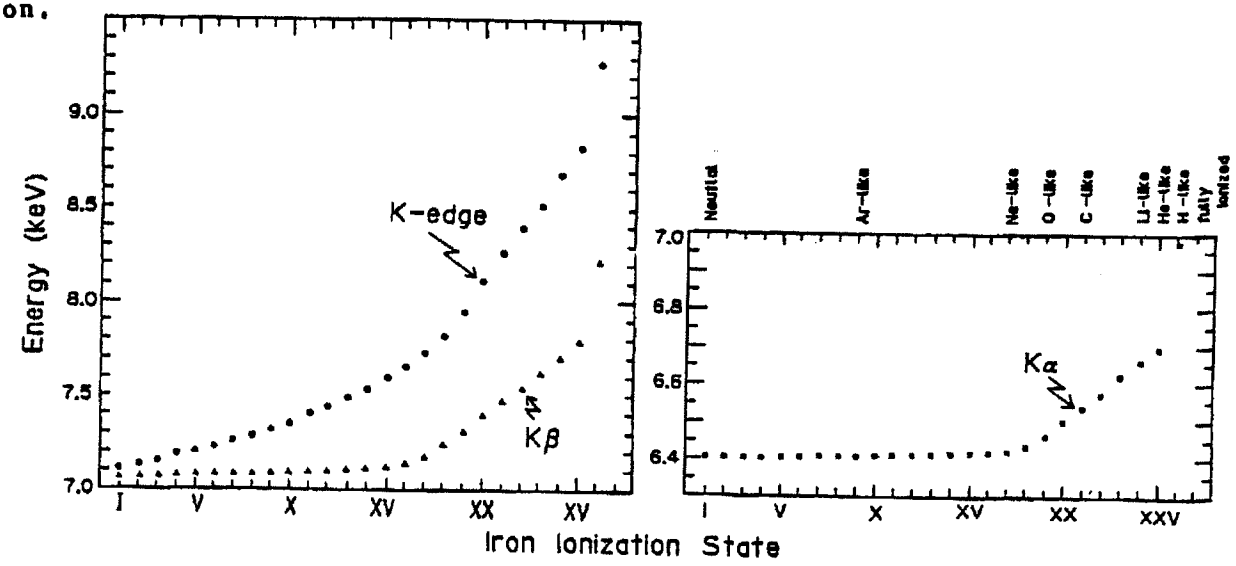

Fig.1 Iron K-edge energy and K-beta line energy (left), and K-alpha line energy (right) as a function of the ionization degree.

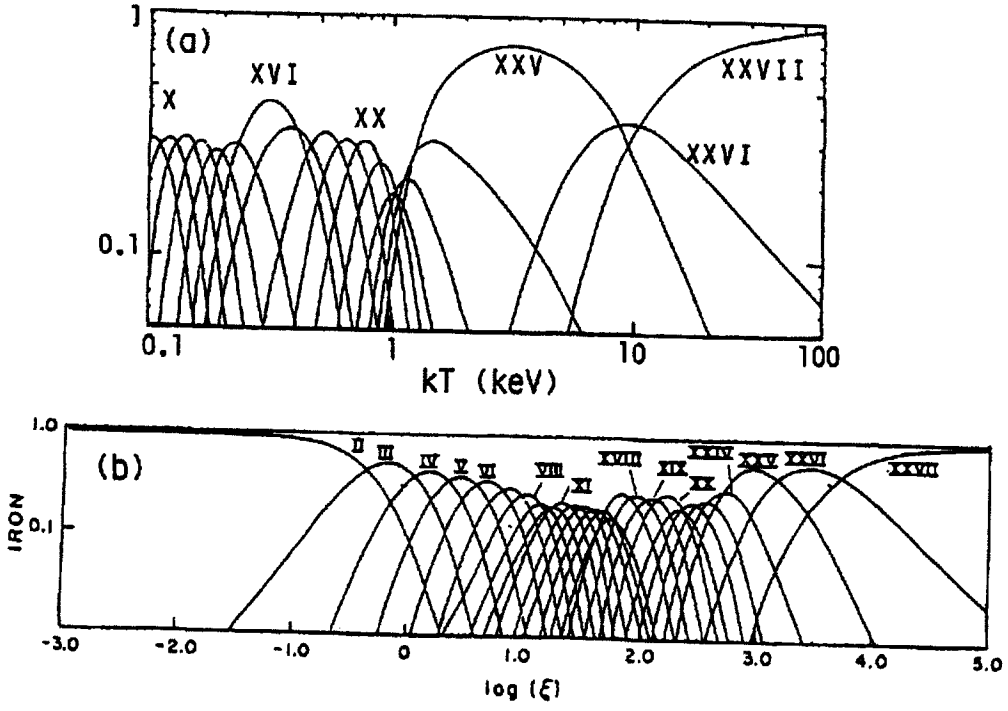

Fig.2 Relative ionization population of iron assuming;
(a) collisional thermal equilibrium, or
(b) photoionization-recombination equilibrium in an X-ray irradiated matter with a small optical depth [K&M82].

II. Iron K-edge Absorption

The iron K-edge absorption feature, regarded mostly as local to the source rather than interstellar, was observed by Tenma from the sources listed in Table 2. Examples of such X-ray spectra are shown in Fig.3. In all cases the K-edge energy was consistent with 7.2 - 7.4 keV. Comparison of this with Fig.1 indicates that the absorbing iron is of low ionization degree (Fe III-X) and thus relatively cool (e.g. $kT < 10^5$ K if in collisional equilibrium).

Source	Edge energy (keV)	References
GX301-2 (high absorption)	7.36±0.02	[MLK85]
Vela X-1 (high absorption)	7.24±0.03	[OHA84a,NAG86]
Her X-1 (near turn-off)	∿7.2	[OHA84b]
Cyg X-1 (dips at sup.conj.)	7.18±0.18	[KIT84]
Cen A (1984 Mar.29-Apr.4)	7.2±0.2*	[WAN86]
NGC4151 (1984 January,March)	∿7.2 *	[MAT86]

* Corrected for cosmological redshift.

Table 2 Energy of the iron K-edge absorption feature measured with Tenma.

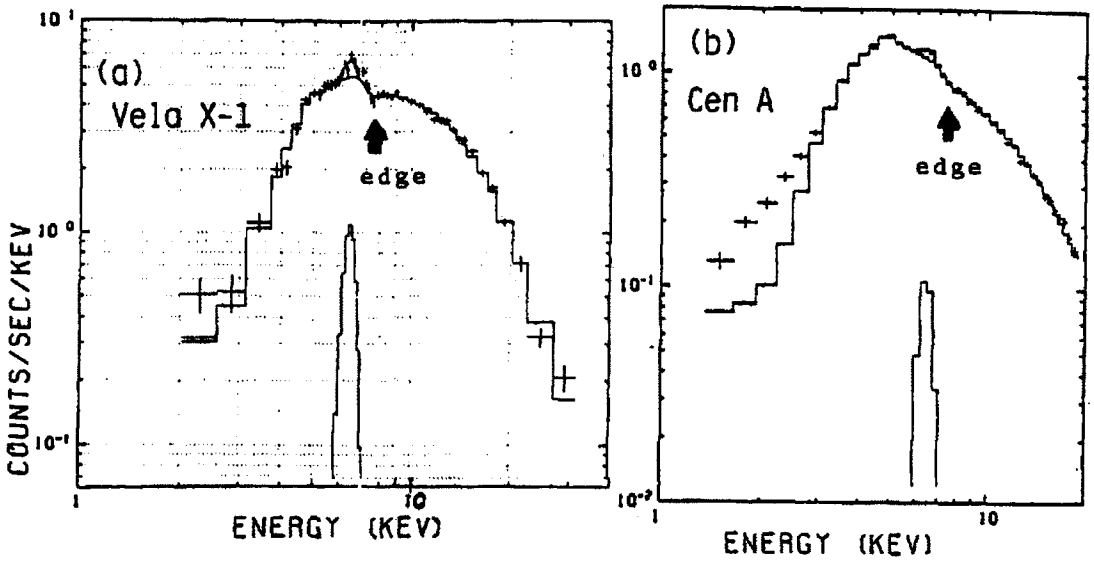

Fig.3 Spectra with iron K-edge absorption feature, observed from Vela X-1 [NAG86] and Cen A [WAN86]. Observed raw spectra (crosses) are fit with a power-law continuum plus a Gaussian line representing the iron K-line emission.

The measured iron edge depth gives the line-of-sight iron column density N_{Fe}. This can be compared directly with the value of N_H determined from the low energy (< 4 keV) absorption of the spectrum, assuming that both N_{Fe} and N_H reflect one and the same material. Here N_H refers to the equivalent hydrogen column density assuming the cosmic abundance [M&M83]. Note that the absorption in the 2-4 keV range is mostly due to O, Ne, Mg, Si, S, Ar, and Ca [M&M83]. Therefore we are effectively comparing the iron abundance relative to these elements. Also note that the inferred ionization degree of iron (Figs.1,2) implies that these medium-light elements also remain in relatively low ionization states, so that the overall photoelectric absorption cross section should not differ significantly from the purely neutral case.

Figure 4 is a scatter plot between the observed values of N_{Fe} and N_H. From this we conclude that the iron abundance is consistent with the "cosmic" value ($N_{Fe}/N_H=3.3\times10^{-4}$ [A&E82]) for all these sources, within an uncertainty of about factor 2.

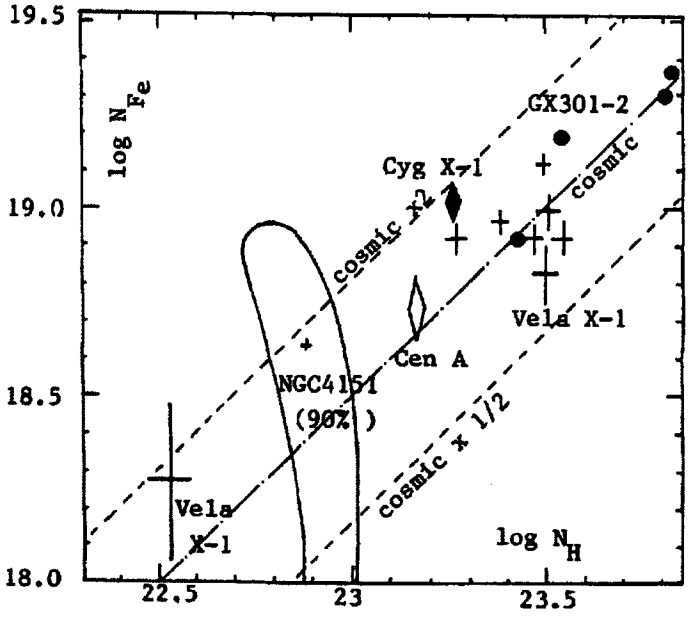

Fig.4 A comparison between N_{Fe} (determined from the iron K-edge depth) and N_H (from the low-energy absorption). For the chemical composition of the matter contributing to N_H the cosmic abundance is assumed, except for iron which is not included in N_H.

III. Fluorescent Iron K-line Emission from Cool Material

(III-1) Observational overview

We observed iron K-emission lines from many massive galactic binaries and a few AGNs [MAK84,KOY85,INO85a,MAT85,TAN86]. As listed in Table 3, the line-center energy was determined mostly to be 6.4-6.5 keV. From these results and Fig.1 we know that the observed lines are coming from low-ionization (Fe I-XIX), cool ($T<10^5$ K) iron ions. Note that the precise line energy determination was enabled for the first time by the GSPC.

Source	Line energy (keV)	Equivalent width (ev)	References
GX301-2	6.46±0.02	200-2000	[MLK85]
Vela X-1	6.42±0.02	70- 400	[OHA84a,NAG86]
Cen X-3	6.4 - 6.6$	100- 200	[KOY85]
Her X-1	6.41±0.05	100- 200	[OHA84b]
OA01657-415	6.48±0.05	220	
4U1700-37	6.5±0.1	150- 250	[MUR84]
4U1538-52	6.4±0.2	< 70	[MAK86]
A0535+26	6.6±0.2	∿100	
Cyg X-1	6.53±0.09	50	See §III-6
NGC4151	6.39±0.07*	320	[INO85b,MAT86]
Cen A	6.46±0.08*	90	[INO85b,WAN86]

* Corrected for cosmological redshift.

$ Line energy varies across pulse phase [KOY85].

Table 3 Summary of observations of iron K-line emission. The iron line was undetectable in two peculiar pulsars X0331+53 and 4U1626-67.

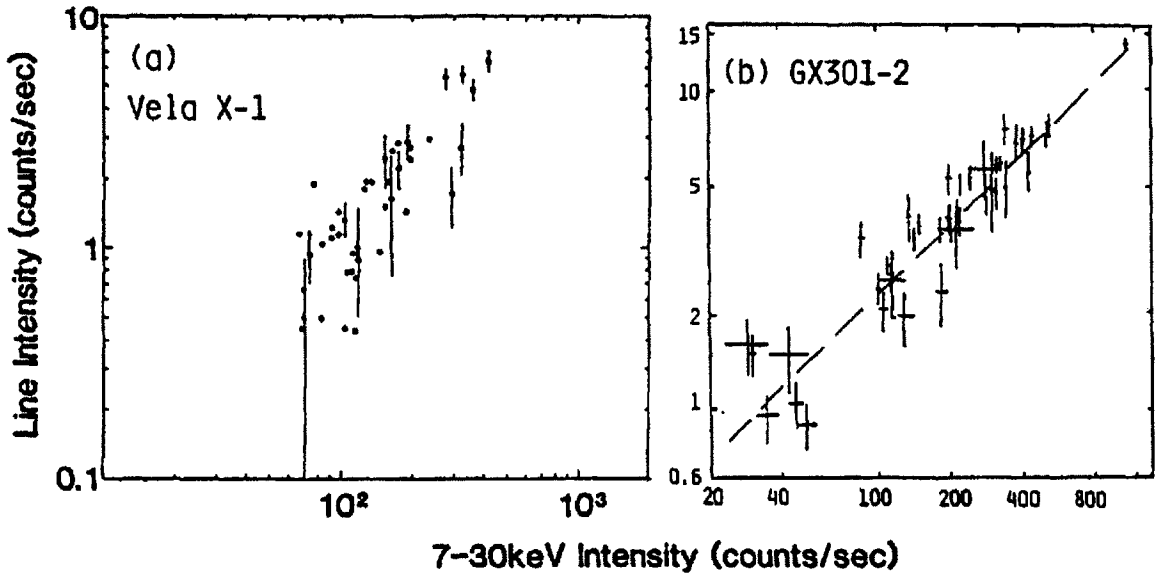

Fig.5 Correlation between the observed iron-line photon flux and the observed continuum X-ray flux above the neutral iron K-edge energy (7.1 keV). These results indicate a fluorescence origin for the iron lines. (a) Vela X-1 [OHA84a]; (b) GX301-2 [MLK85]

The observed line equivalent width varied considerably, from source to source, and even from observation to observation for each individual source. However there exists, as shown in Fig.5, a rough proportionality between the observed line photon flux and the observed continuum flux above 7.1 keV (which can ionize the neutral iron atoms by K-photoionization, followed by fluorescent K-line emission). This indicates that these iron lines are produced through the fluorescent reprocessing of continuum X-rays from the central power source by the cool matter surrounding it. There is no significant difference in this respect between galactic and extragalactic sources.

(III-2) Matter distribution around X-ray sources

We often observed K-line emission and K-edge absorption at the same time (Fig.3), and the line and edge energies always indicated a consistent ionization degree. We thus assume that the same matter is causing the absorption and the fluorescent line emission. Then, the observed X-ray spectrum can be decomposed into three distinct components in reference to Fig.6 [KOY85,INO85a], ignoring other lines;

(i) direct-beam continuum

$$I(E;N_0) = f(E,\vec{e}_0)\cdot \exp[-\sigma(E)N_0] \qquad (1)$$

(ii) Thomson-scattered continuum

$$J(E)= \int_0^\infty dr \int \frac{d\vec{e}}{4\pi} \exp[-\sigma(E)(N_1+N_2)]\cdot \sigma_T n(\vec{r})\cdot f(E,\vec{e}) \qquad (2)$$

(iii) fluorescent K-line emission

$$L = \delta(E-E_K)\int_0^\infty dr \int \frac{de}{4\pi}\int_{z.l}^\infty dE'\cdot \exp[-\sigma(E')N_1-\sigma(E_K)N_2]\cdot \alpha\omega\cdot\sigma_{Fe}(E')n(\vec{r})f(E',\vec{e}) \qquad (3)$$

Here $f(E,\vec{e})$ is the continuum emitted from the central source with E the photon energy and $\vec{e}$ the directional unit vector, $n(\vec{r})$ is the local matter number density around the source, σ_T is the Thomson cross section, $\sigma(E)$ is the total photoelectric absorption cross section assuming the cosmic abundance [M&M83], σ_{Fe} is that due to neutral iron, $\alpha = 3\times10^{-4}$ is the cosmic iron abundance, $\omega = 0.34$ is the K-fluorescence yield, E_K is the K-line energy, and N_0, N_1 and N_2 are the column densities of the matter as specified in Fig.6.

The second and the third components above were evaluated by the

Monte-Carlo simulations [OHA84a,KOY85,INO85a,MLK85], and a few examples are presented in Fig.7. The scattered component is negligible as compared to the direct one only when the Thomson opacity of the cloud is << 1. The scattered continuum is somewhat more absorbed than the direct continuum, reflecting its longer effective path length within the matter cloud. The scattered continuum, being a superposition of many different scattering paths with different optical depths, differs in detailed shape from the direct continuum : notice $\langle \exp(-\tau) \rangle \neq \exp(-\langle \tau \rangle)$ in general, where τ is the opacity and $\langle\ \rangle$ means the geometrical average.

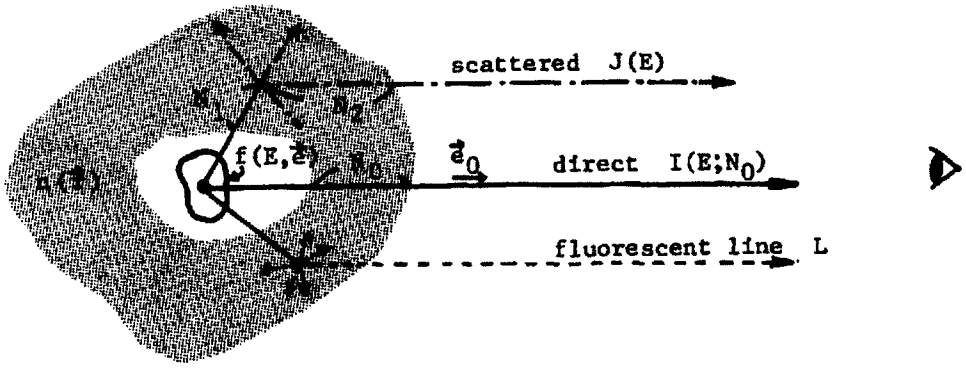

Fig.6 A schematic of the radiation transfer in cold matter around a compact X-ray source.

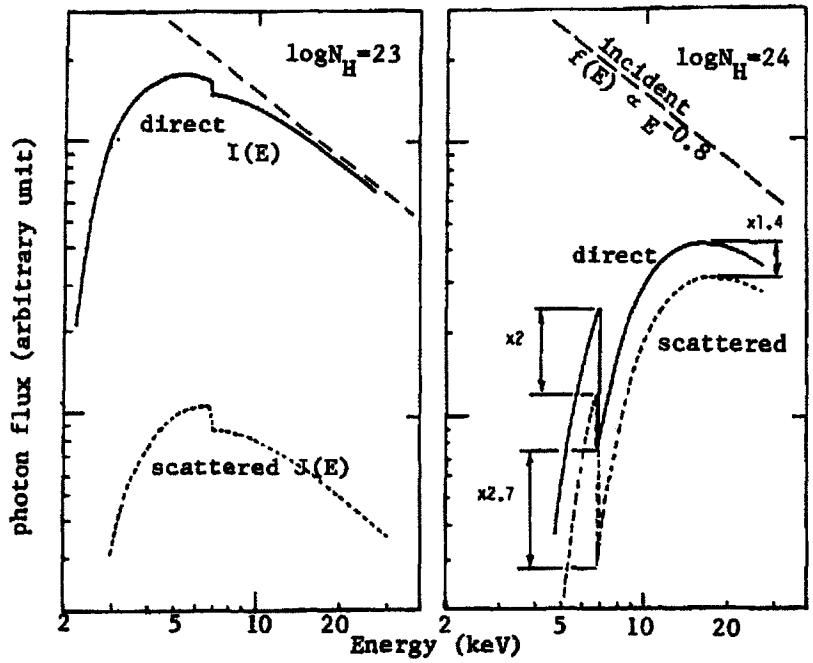

Fig.7 Scattered continuum spectra, calculated using Monte-Carlo method for an isotropic incident photon spectrum of the form $E^{-0.8}$ [NAK86]. The matter distribution around the central source is assumed uniform and isotropic, with radial column density N_H. The direct continuum is also presented for comparison.

(III-3) Line equivalent width -- calculation

To compare with the observation, we calculated by the above Monte-Carlo method the expected line equivalent width (E.W.) as a function of the matter thickness [KOY85,INO85a,MLK85]. For the chemical composition we assume the cosmic abundance. In Fig.8 we show, after [KOY85], the results for several representative cases.

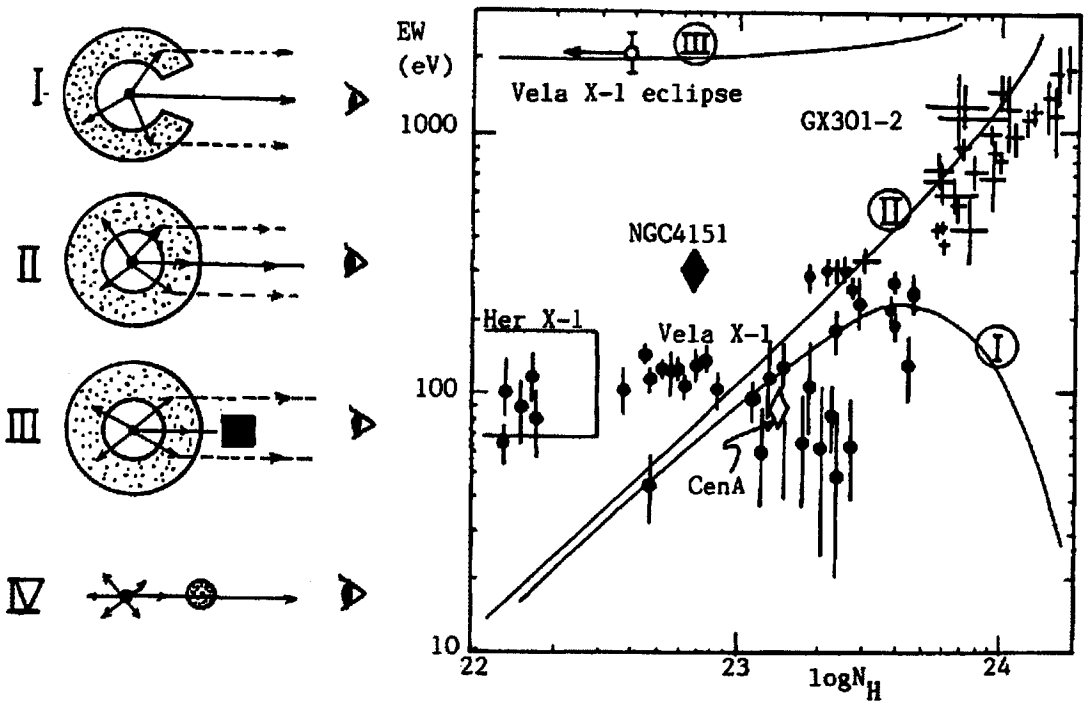

Fig.8 Relation (solid line) between the matter thickness N_H and the iron line equivalent width calculated by Monte-Carlo method for the representative Models I-III illustrated on the left. On the same diagram, the observed E.W. and the observed line-of-sight absorption column are plotted for comparison.

Model I corresponds to the definition of E.W. as

$$\text{E.W.} = L/f(E_K,\vec{s}) \quad . \tag{4}$$

This implies a situation when the absorption somehow avoids the line of sight. In this case the line equivalent width reaches the maximum value of ~180 eV at about $N_H=10^{24}$ cm^{-2}, beyond which it decreases due to self absorption. Model II is the simplest one, when an uniformly distributed matter causes the line-of-sight absorption as well as the scattering and fluorescence. This corresponds to the definition as

$$\text{E.W.} = L/[\ I(E_k;N_0) + J(E_K)\ ] \quad . \tag{5}$$

The E.W. then increases almost linearly with increasing N_H.

Model III assumes that the direct beam is completely blocked by some thick material (e.g. the companion star). Then the definition of E.W. becomes

$$E.W. = L/J(E_K) . \qquad (6)$$

In this case E.W. is nearly constant, at $\sim$2 keV, for a wide range of N_H. This is easily understood by comparing eqs.(2) and (3), where the radiative transfer relations are very similar between the two processes. Finally in Model IV the matter is assumed to be localized along the line of sight, so that it causes significant absorption but little scattering or fluorescence.

(III-4) Line equivalent width -- observation

The four cases introduced in §III-3 are in fact found in the observation [KOY85]. In Fig.8 we plot the observed E.W. (defined as the ratio between the observed line photon flux and the observed continuum at 6.4 keV) against observed line-of-sight absorption N_H. Shown in Fig.9 are the corresponding spectra. For GX301-2 the observed E.W.-N_H relation is in good agreement with the prediction by Model II [W&S84, MLK85], indicating that this pulsar is imbedded in a dense, almost uniformly distributed cool matter. This matter can be identified with the dense stellar wind from the supergiant primary star Wray 977 [PAR80]. The data for Cen A are also consistent with this case.

Figure 9c shows a series of spectra from Vela X-1 during its eclipse ingress [SAT86]. The ingress is characterized by an increasing absorption and scattering. At the mid eclipse, however, the spectrum is no longer strongly absorbed and the iron line is very prominent (E.W. $\sim$2 keV). This exactly corresponds to the Model III in Fig.8; the direct beam is stopped by the supergiant companion, while the stellar wind and the companion's atmosphere produce the scattered continuum and the fluorescent line. See §III-5 for further details.

Figure 9d is a spectrum of Cyg X-1 during "dip" events near the superior conjunction [KIT84]. A deep iron K-edge absorption is seen, but the iron line emission is nearly absent. This is an ideal example of Model IV [KOY85], implying that the dense matter ejected from the primary temporarily came into our line of sight. See also §III-6.

In Fig.8 we see that the E.W. for Her X-1 and Vela X-1 remains 100-150 eV even when the line-of-sight N_H is very small. Figure 9a gives an example of such spectrum. This may be interpreted, in terms of Model I,

that there exists some thick "target" material outside our line of sight. The observed E.W. is nearly the same as the maximum value expected from Model I, suggesting that the target covers a significant fraction of the solid angle containing the pulsed X-ray beam.

NGC4151, with it unusually large E.W., is the most puzzling case. We discuss this case later in §III-8.

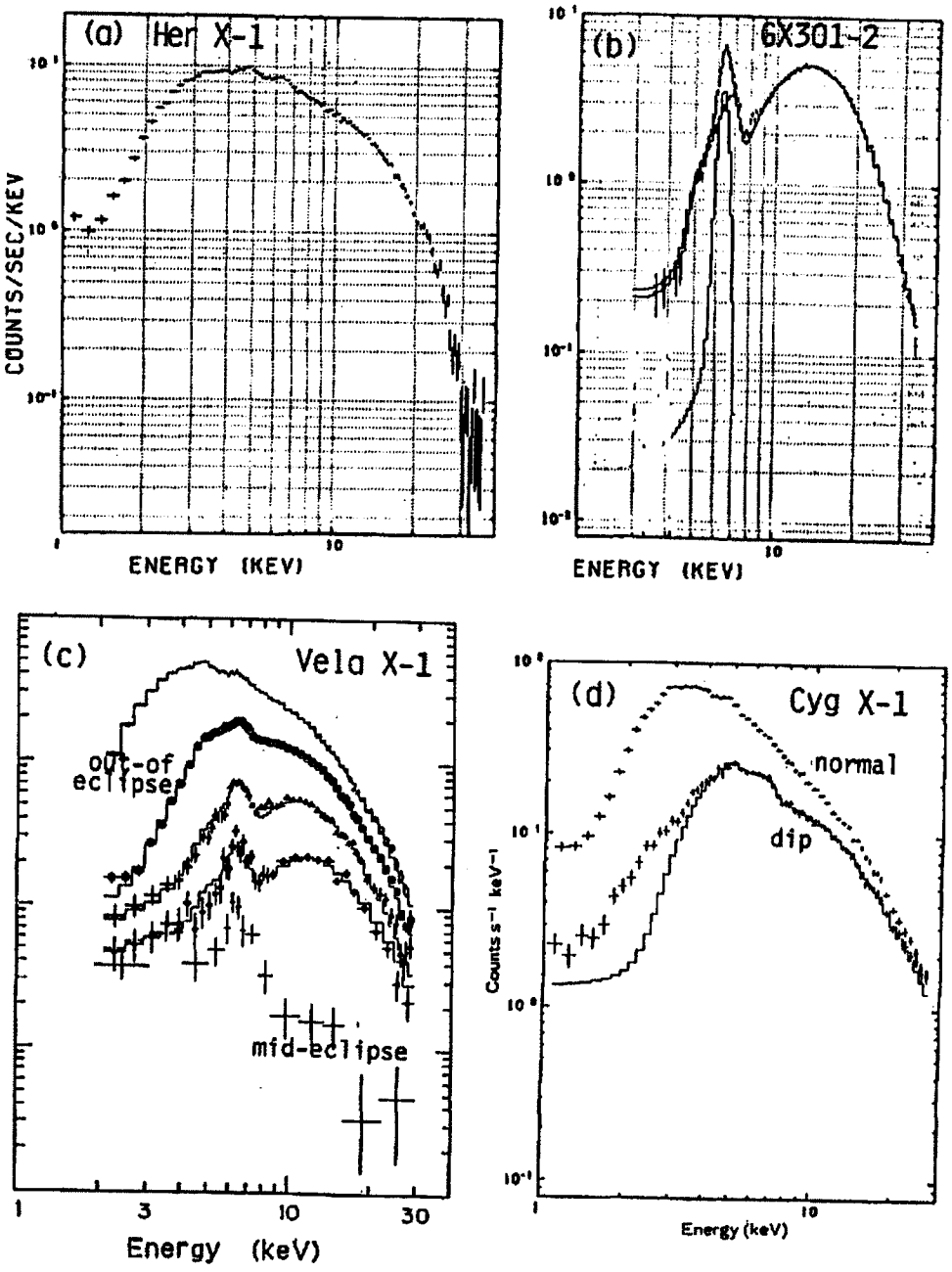

Fig.9 X-ray spectra corresponding to the Models I-IV of Fig.8.
(a) Her X-1 (Model I) [OHA84b].
(b) GX301-2 (Model II) [MLK85].
(c) Vela X-1 during eclipse ingress (Model III) [SAT86]
(d) Cyg X-1 near the superior conjunction (Model IV) [KIT84].

(III-5) Origin of fluorescent line emissions from X-ray pulsars

Figure 10 shows the orbital-phase variations of the iron line intensity from Vela X-1 [OHA84a,NAG86,SAT86]. As already shown in Fig.9c, we observed a significant (∿15%) residual line emission during the eclipse periods ; a certain fraction of the iron line flux is in fact produced in regions comparable in size to the companion star (~10^{12} cm) [OHA84a]. Such regions may be identified with the stellar wind from the primary and the photosphere of the primary itself.

In Fig.10 we calculated the expected contributions from these two regions, in which the detailed radial structures of the primary's atmosphere and of the stellar wind have been modelled based on the observed changes of the continuum spectrum along the eclipse transitions (Fig.9c) [SAT86]. Although the observation is fairly well simulated, the model still falls short of the observed out-of-eclipse line intensity and fails to reproduce the abrupt jump at the eclipse ingress and egress. These discrepancies are nicely solved if we assume a third component with E.W. ∿80 eV, local to the pulsar thus showing a sharp eclipse transitions. This localized matter should be identified with the fluorescing "target" mentioned in §III-4.

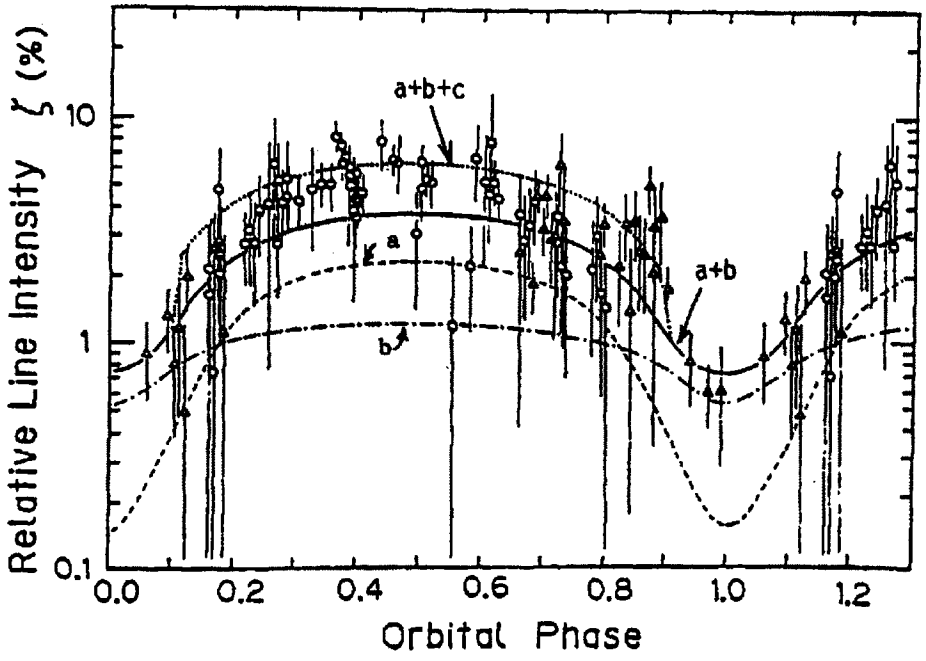

Fig.10 The binary phase dependence of the iron line intensity observed from Vela X-1, in comparison with calculation [SAT86]. The "relative line intensity" is proportional to the E.W. as defined by eq.(4) in the text. Curves a and b represent the calculated contributions from the primary's atmosphere and the stellar wind, respectively. The curve labeled as a+b+c assumes another reprocessing region close to the pulsar.

From these results we conclude that there are three distinct regions in Vela X-1 producing fluorescent iron lines ;
(i) The atmosphere of the primary supergiant HD77581 (E.W. $\lesssim$ 60 eV);
(ii) The stellar wind from the primary (E.W. $\sim$ 30 eV) ; and
(iii) A matter localized close to the pulsar (E.W. $\sim$80 eV).
The case of Her X-1 and Cen X-3 seems similar [KOY85], while in GX301-2 the second component seems dominant. The physical reality of the third component is yet to be investigated, but it is very likely to be matter on the Alfven shell [IN085a].

We found that the iron line intensity from Vela X-1, GX301-2 and Her X-1 were effectively free from pulse modulation [OHA84a,MAK84]. The case of GX301-2 may be explained by the approximate isotropy of the fluorescing matter distribution, which will geometrically average out local pulse modulations in the fluorescent flux. For Vela X-1 and Her X-1, however, we already know that the matter distribution cannot be isotropic, since the component (iii) above must be located outside the line of sight between us and the pulsar. Then the absence of line intensity modulation requires that the local "target" matter corotates with the pulsar [IN085a]. This reinforces the above suggestion that the "target" matter may be identified with the matter on the Alfven shell.

(III-6) Cyg X-1

Cyg X-1 is believed to be a black hole binary but otherwise is very similar to ordinary massive neutron-star binaries. It is therefore very important to study its iron line emission in comparison with those from the X-ray pulsars. The iron K-line intensity from Cyg X-1, observed by EXOSAT [BWP85] as well as Tenma (Table 3), is significantly weaker than those from the binary X-ray pulsars. A self-consistent explanation, then, is that Cyg X-1, containing a black hole instead of a magnetized neutron star, lacks the Alfven surface and hence lacks the reprocessing region (iii) mentioned in §III-5. Thus the results of iron line spectroscopy argue favourably for the black hole scenario for Cyg X-1.

The EXOSAT observations of Cyg X-1 also showed that a single power-law fit to the observed continuum requires a broadened (and possibly red-shifted) line component [BWP85]. Such intrinsic line widths would allow several alternative explanations, including ; (1) blend of many lines from different ionization species; (2) Compton broadening; (2) Doppler broadening; etc. In fact the EXOSAT results were interpreted in terms of Comptonization by the disk corona. However, as shown below,

such line broadening should be treated with extreme caution (Table 1).

As shown in Fig.11, the Tenma data for Cyg X-1 closely resemble the EXOSAT data, indicating that the two observations are consistent. Yet, it should be kept in mind that the assumption of a single power-law continuum may not be adequate at the level of data accuracy concerned. Some fraction of the continuum may undergo scattering and may bear a noticeable iron K-edge absorption feature (Fig.7). When this possibility is taken into account, the observed data no longer require the line broadening (Fig.11c). Thus the broad iron line is not an unique interpretation of the Cyg X-1 data, but instead is merely one of several possible alternatives of similar likelihood.

In short, we would easily get false line broadening if the continuum model was only slightly wrong, and such broadening would lead to a serious overestimation of the line equivalent width. This caution should also be applied to the low-level 6.7 keV emission lines from low-mass X-ray binaries [SUZ85,INO85a,WHI86].

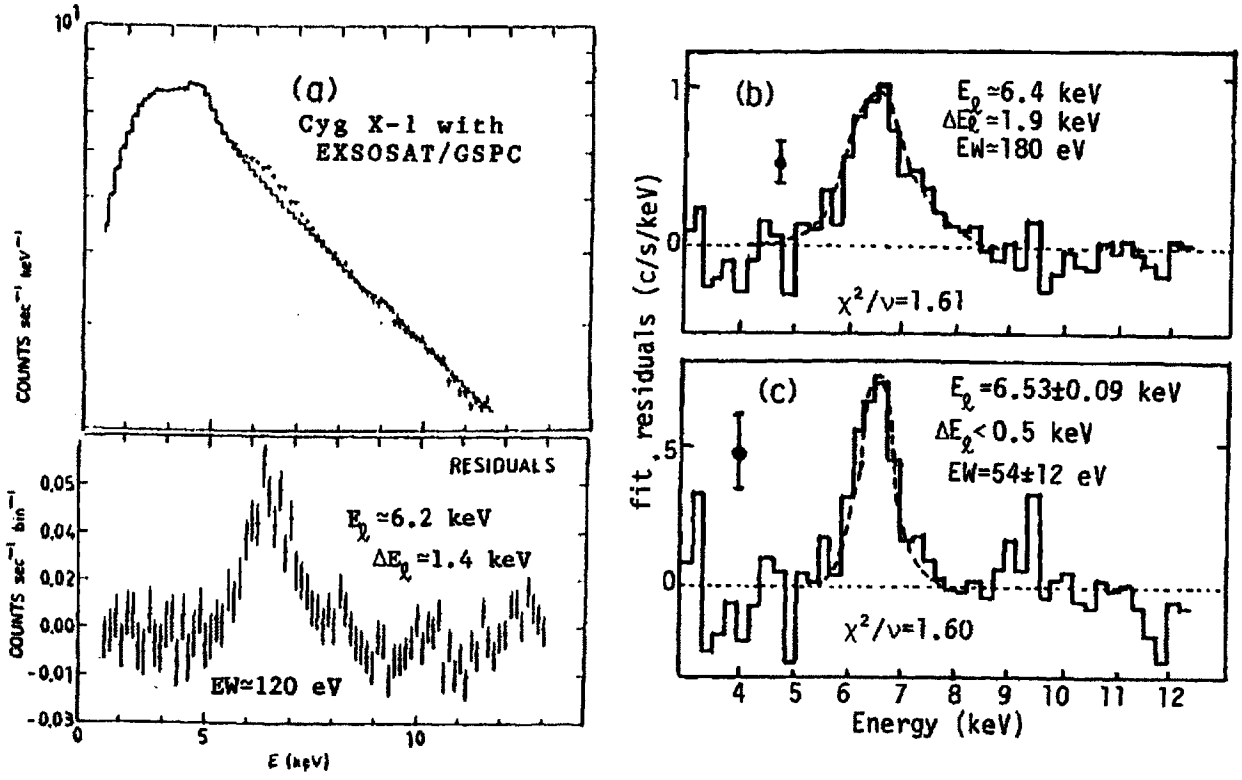

Fig.11 Iron lines from Cyg X-1 observed by Tenma and EXOSAT.
(a) The broadened iron line profile obtained by the EXSOAT GSPC [BWP85], after subtracting the best-fit power-law continuum.
(b) The same as panel (a), but using the Tenma GSPC data. Note that the profile is quite similar to that in panel (a).
(c) The same data as panel (b), but assuming that 20 % of the continuum undergoes absorption by 2.4×10^{23} cm^{-2} and the rest by 1.4×10^{23} cm^{-2}. A narrow line model gives a fit chi-square as good as in panel (b).

(III-7) Anisotropy in the matter distribution : case of GX301-2

Although we have seen that GX301-2 is generally described by the Model II (isotropic matter distribution) of Fig.8, some of its spectra are actually in significant deviation from this situation. Figure 12a is one such example, where the observed line E.W. is in excess of the prediction based on the observed absorption. Furthermore, its spectral shape immediately above the iron K-edge cannot be expressed by a single value of N_H. These imply that the isotropic matter distribution is only an approximation even for GX301-2, and that we must sometimes take into account the possible matter anisotropy. Such anisotropy would first manifest itself as a difference between the line-of-sight column density N_0, contributing to the absorption, and the matter thickness averaged over 4π, denoted $\langle N_H \rangle$, causing scattering and fluorescence.

The above idea may be formulated by referring to eqs.(1)-(3) and Fig.6, and introducing a model photon spectrum of the form [NAK86]

$$I'(E\ ;\ N_0, \langle N_H \rangle\ ) = I(E;N_0) + J(E;\langle N_H \rangle) + L(\langle N_H \rangle)\ . \qquad (7)$$

For the incident continuum f(E) we employed the conventional "power-law plus exponential cutoff" model with 4 free parameters [WSH83]. Including N_0 and $\langle N_H \rangle$, the present model thus involves 6 free parameters. Note that Fig.12a corresponds to the case of $N_0 = \langle N_H \rangle$.

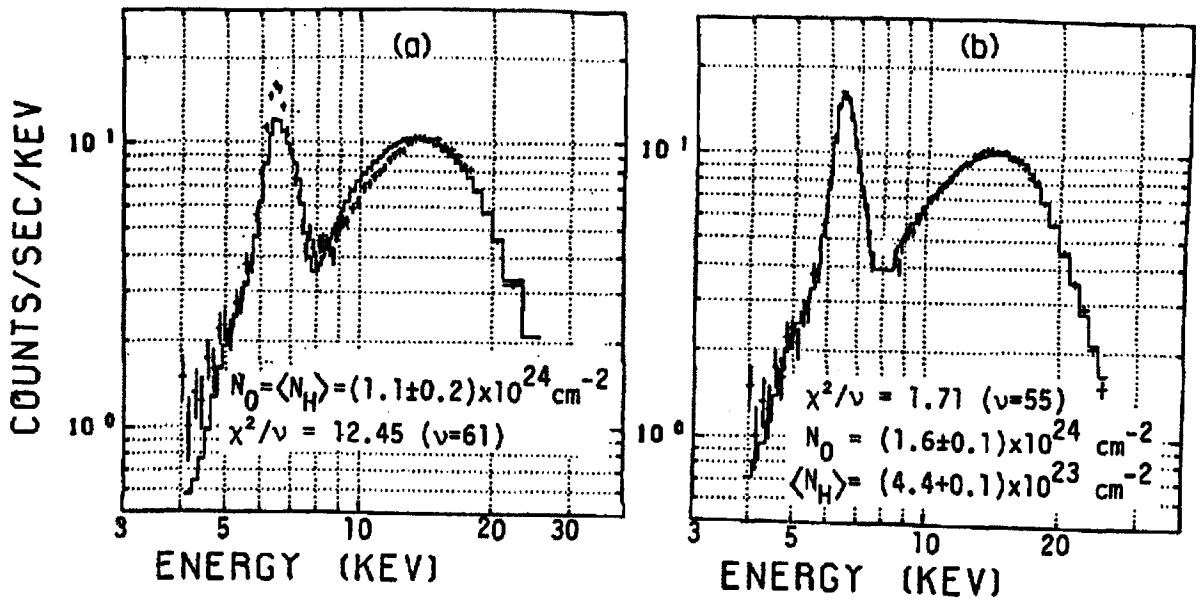

Fig.12 Fitting of the same pectrum from GX301-2 to the model of eq.(7) [NAK86]; (a) under the constraint of $N_0 = \langle N_H \rangle$, where N_0 is the line-of-sight absorption column, and ; (b) When N_0 and $\langle N_H \rangle$ are allowed to vary independently. In either case the iron line intensity is not a free parameter but constrained by $\langle N_H \rangle$, the column density of matter averaged over 4π.

When the spectra of GX301-2 were fit with eq.(7), $N_0/\langle N_H \rangle$ was found mostly in the range between 0.5 and 2 [NAK86]. Such small difference between N_0 and $\langle N_H \rangle$ may be explained by the inhomogeneity in the stellar wind density [NAK86,NAG86]. However we sometimes found much larger ($\gtrsim$factor 3) difference between them. For example, the spectrum of Fig.12 requires $N_0/\langle N_H \rangle \approx 3.7 \pm 0.1$. These cases also include an eclipse-like phenomenon of GX301-2 lasting $\lesssim$ 1 hour, when the continuum flux became very weak while the iron line remained very strong [KOY85,MLK85, LEA86,NAK86]. This translates into an abrupt increase in N_0 (from 6×10^{23} to 6×10^{24} cm^{-2}), while $\langle N_H \rangle$ remained roughly constant at $(2-4) \times 10^{23}$. This event may possibly be caused by a dense tail-shock front, which blocked most of the direct continuum thus making the situation similar to the Model III in Fig.8.

(III-8) Active galactic nuclei

As shown in §III-4 and Fig.8, we detected 6.4 keV iron K-lines from two AGNs, Cen A and NGC4151 [INO85b,MAT86,WAN86]. The line E.W. for Cen A is consistent with the prediction based on the observed line-of-sight absorption (Model II of Fig.8), while that for NGC4151 exceeds the prediction so much (by factor 6) that the data cannot be accounted for even by invoking a highly anisotropic matter distribution around [INO85, MAT86]. An ad-hoc assumption of iron overabundance would be inconsistent with the conclusion made in §II. One possible solution for NGC4151 is to assume that the continuum flux from its nucleus is strongly beamed so that we observe only a small fraction of it ("missing beam" assumption) [INO85a,MAT86].

An alternative explanation was suggested during the conference. Dr. M. Morini, combining the EXOSAT and Tenma observations, showed that the iron line intensity of Cen A may be less variable than its continuum intensity on time scales of months to years. Also Dr. M. Penston pointed out that the case of NGC4151 (Fig.8) may be due to the fact that it was unusually faint in X-rays during the Tenma observations (January and March 1984) [PEN86]: the line intensity may not follow these short-term excursions in the continuum intensity. These suggestions imply that the fluorescent reprocessing region in the AGN has a physical size of 10^{17-18} cm and the line variation is smeared out by the light-travel-time effect. This size nicely coincide with that of the BLR (broad line region), indicating that the flourescence may take place in the BLR.

IV. Iron K-line Emission from Thin Hot Plasma

(IV-1) Observations

The optically thin, hot plasma is also a very good candidate of the X-ray emission line spectroscopy. This situation has been encountered in a wide variety of celestial objects, including; (1) supernova remnants; (2) clusters of galaxies [OKU86]; (3) white-dwarf binaries; (4) star-forming regions (ρ-Oph, Orion Nebula [AGR86] etc.); and (5) galactic-ridge excess emission [KOY86, WAR85]. Figure 13 shows several examples.

By measuring accurately the energies of emission lines in these spectra, we can evaluate whether the plasma is in ionization equilibrium or not. If so then the iron line should show up at about 6.7 keV for a wide range of the plasma temperature concerned, due to the predominant stability of the helium-like iron ions (Fig.2a). To examine this we plot in Fig.14a the observed iron line energies against the measured plasma temperature (assuming a thermal bremsstrahlung continuum). It indicates that these sources are more or less in the ionization equilibrium, except for the two SNRs Cas A and Tycho.

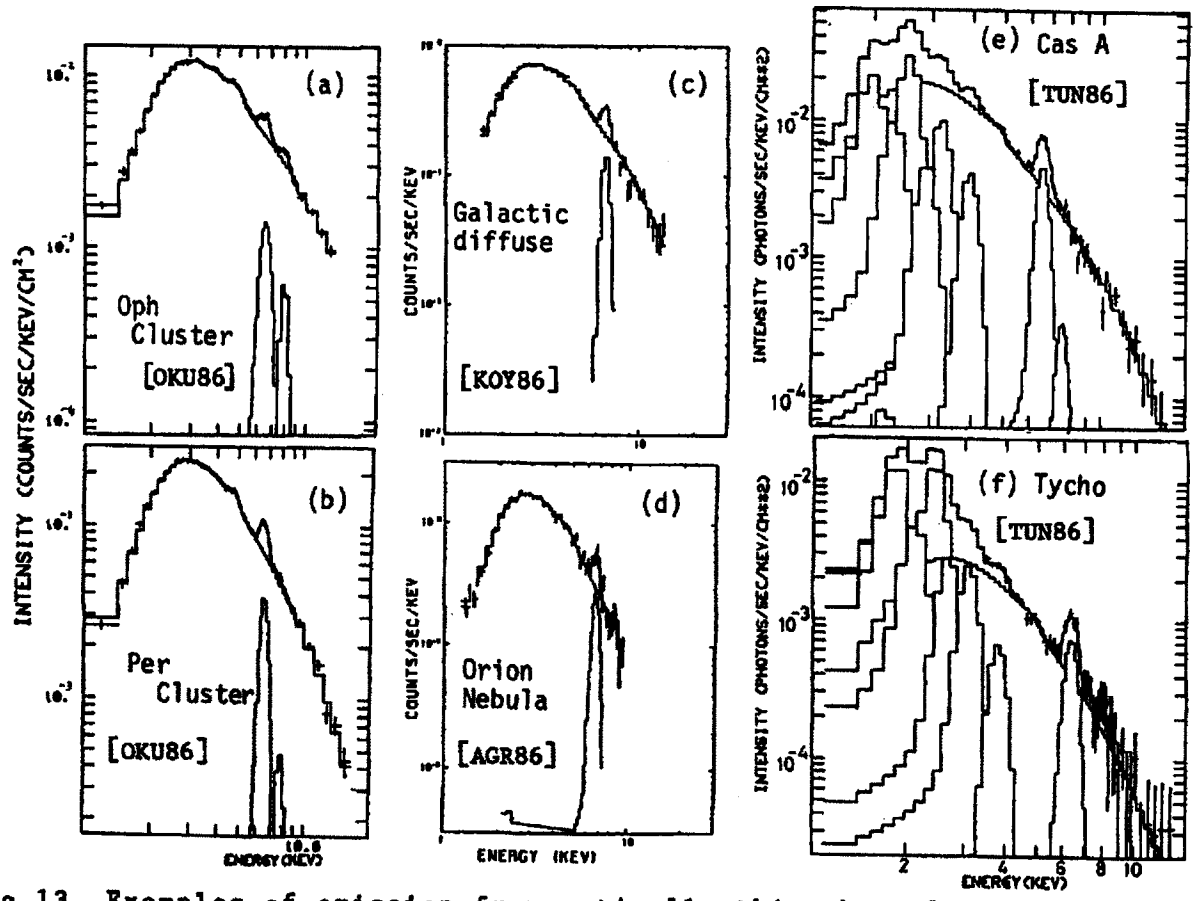

Fig.13 Examples of emission from optically thin, hot plasma.

(IV-2) Case of ionization equilibrium

When the plasma is in the ionization equilibrium, we can estimate the abundances of elements such as Si, S, Ar, Ca and Fe by comparing the observed line E.W. with the calculations [R&S77]. As shown in Fig.14b the iron in these sources is roughly consistent with, or somewhat less than, the cosmic abundance.

The spectrum of the Coma cluster of galaxies was examined closely for any non-isothermal indication, but the result was rather negative in the sense that the data are consistent with both the isothermal and adiabatic models [HUG86]. This contradicts the previous claim for the non-isothermality in the Coma cluster [H&M86].

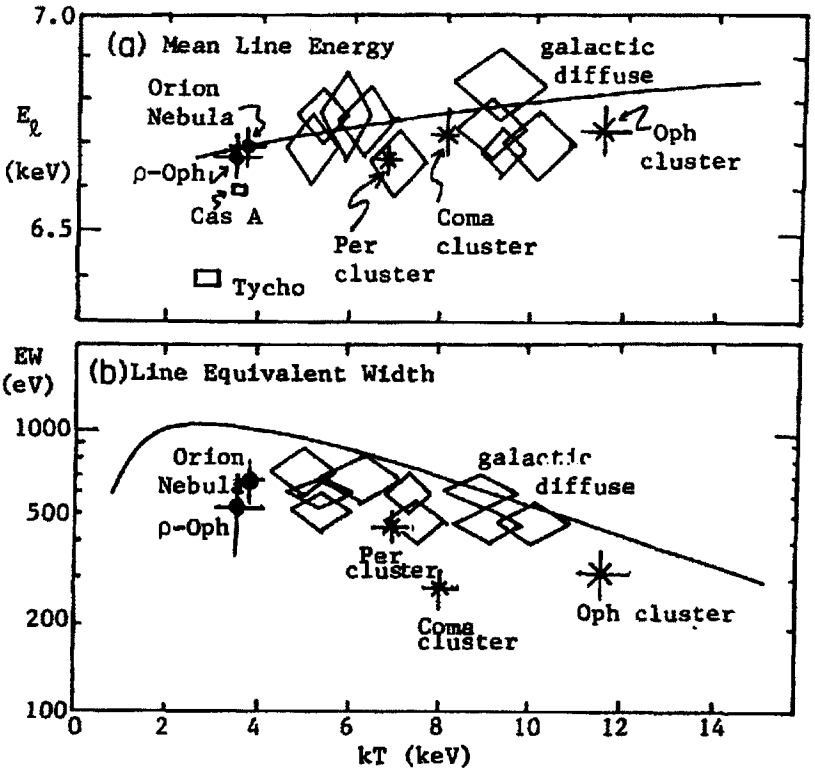

Fig.14 The observed iron K-alpha line energy (panel a) and line E.W. (panel b) plotted against the observed plasma temperature. In both panels the solid curve shows the calculation assuming the ionization equilibrium and the cosmic abundance of iron.

(IV-3) Case of ionization non-equilibrium

In Figs.13e and 13f we present the spectra of two SNRs, Cas A and Tycho, observed from Tenma [TUN86]. In addition to the iron K-alpha line, many other emission lines are identified; see Table 4. The Tycho's SNR exhibits systematically lower emission line energies than Cas A,

despite little difference in the plasma temperature. This indicates that the plasma in Tycho is less ionized as compared to that in Cas A. In fact, these observations have been successfully interpreted in terms of the ionization non-equilibrium model (Fig.15) [MAS84].

These two SNRs exhibit much stronger silicon and sulfur lines as compared to the other sources in Fig.13. This is partly due to the ionization non-equilibrium condition, and partly to the enhanced abundance of heavy elements in these sources as a consequence of nucleosynthesis in the progenitors. Detailed discussion and comparison with the Einstein SSS data are found in [TUN86].

		Cas A	Tycho	helium-like	hydrogen-like
Si	K-α	1.94±0.02	1.84±0.02	1.86	2.01
	K-β	2.23±0.08	2.08±0.04	2.18	2.25
S	K-α	2.53±0.03	2.38±0.02	2.46	2.62
	K-β	2.88±0.15	2.65±0.06	2.88	3.11
Ar	K-α	3.18±0.03	3.06±0.02	3.14	3.32
Ca	K-α	3.89±0.02	3.76±0.04	3.91	4.11
Fe	K-α	6.59±0.02	6.40±0.03	6.71	6.93
	K-β	7.67±0.15	---	7.90	8.21

Table 4 Best-fit emission line energies for Cas A and Tycho [TUN86]. K-line energies from helium-like and hydrogen-like ions are also listed.

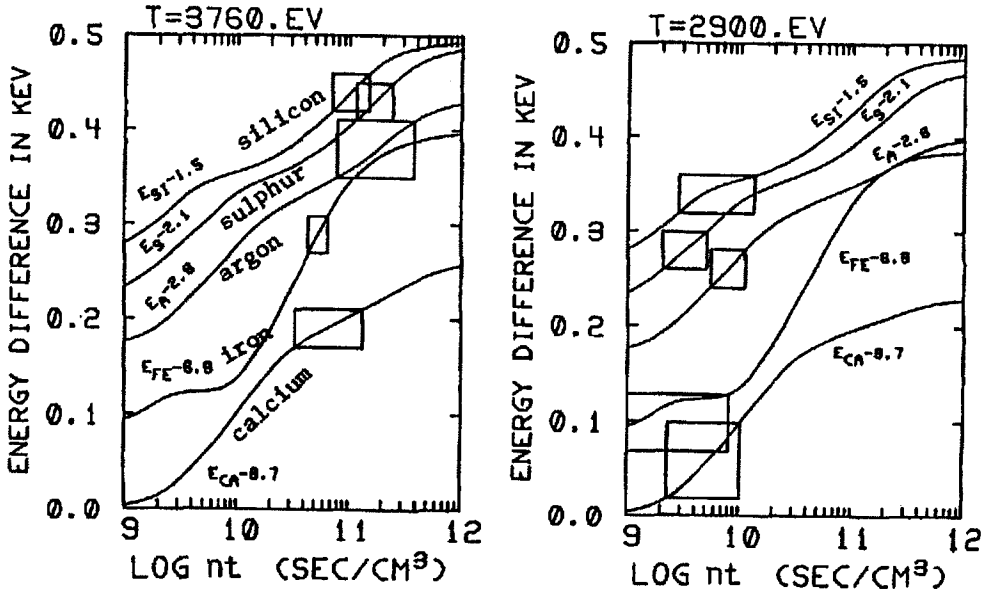

Fig.15 Evolution of the mean energies of various Kα lines, as a function of nt, where n is the plasma density and t is the time after the supernova explosion. Solid curves show the calculation [MAS84] and the boxes represent the observation summarized in Table 4. The line energies are displayed with a constant offset subtracted [TUN86].

V. Summary

Results of the iron line spectroscopy of the galactic and extragalactic X-ray sources, using the Tenma GSPC, are reviewed.

The iron K-edge absorption features, detected in several massive galactic binaries as well as a few AGNs, indicate that the iron abundance in these sources is consistent with the "cosmic" value.

These objects also emit 6.4 keV iron K-lines, which arises due to the fluorescent reprocessing of the continuum X-rays from the central power source by a surrounding cool material. In X-ray pulsars the reprocessing material is identified with the photosphere and stellar wind of the primary star. In some cases, additional matter local to the pulsar (e.g. near the Alfven shell) is required. When matter distributed around the source is dense, scattered continuum must be taken into account to explain the observed X-ray spectra. The fluorescent lines from AGNs may be produced in the broad line region (BLR). These results show that the iron line spectroscopy provides a powerful tool to study the matter distribution around accreting compact objects.

Iron emission lines from optically-thin hot plasma was also widely observed in clusters of galaxies, supernova remnants, star-forming regions etc., as well as in the galactic-ridge excess emission. These data are used to examine the iron abundance and the ionization equilibrium.

Finally there are several topics which could not be included in the present talk. They are; the weak 6.7 keV emission lines from the low-mass neutron-star binaries [SUZ84,KOY85,WHI86]; the enigmatic iron emission lines from Cyg X-3 and Cir X-1 [INO85]; and the case of SS433.

ACKNOWLEDGEMENTS

The present talk has been based on the total activity of the Tenma team rather than the author's personal contribution. He is thus deeply indebted to all the members of the Tenma team. He is above all thankful to Drs. Hajime Inoue and Katsuji Koyama, and to Profs. Masaru Matsuoka, Fumiyohsi Makino, Fumiaki Nagase and Koujun Yamashita, for their valuable discussions and for giving him liberty to use their work (published and unpublished) in the present talk. Also he thanks Dr. E. Fenimore of LANL for the careful reading of the manuscript and valuable comments.

[REFERENCES]

(PASJ = Publ. Astr. Soc. Japan)
(ISAS RN = Research Note of Inst. Space. Astronautical Science)

[A&E82] Anders,E. and Ebihara,M. 1982, Geochim. Cosmchim. Acta **46**, 2363.

[AGR86] Agrawal,P.C, Koyama,K., Matsuoka,M. and Tanaka,Y. 1986, submitted to PASJ (ISAS RN #300).

[BWP85] Barr,P., White,N.E. and Page,C.G. 1985, MNRAS **216**, 65p.

[H&R86] Henriksen,M.J. and Moshotzky,R.F. 1986, Ap.J. **302**, 287.

[HUG86] Hugues,J.P. et al. 1986, manuscript in preparation.

[INO85a] Inoue,H. 1985, Space Science Reviews **40**, 317.

[INO85b] Inoue,H. 1985, Proc. Japan-US Seminar on Galactic and Extra-Galactic Compact X-ray Sources, ed. Y.Tanaka and W.H.G.Lewin (January 1985, Tokyo), Published from ISAS, p.283.

[KIT84] Kitamoto,S., Miyamoto,S., Tanaka,Y., Ohashi,T., Kondo,Y., Tawara,Y. and Nakagawa,M. 1984, PASJ **36**, 731.

[K&M82] Kallman,T.R. and McCray,R. 1982, Ap.J. Suppl. **50**, 263.

[KOY84] Koyama,K. et al. 1984, PASJ **36**, 659.

[KOY85] Koyama,K. 1985, Proc. Japan-US Seminar on Galactic and Extra-Galactic Compact X-ray Sources, ed. Y.Tanaka and W.H.G.Lewin (January 1985, Tokyo), Published from ISAS, p.153.

[KOY86] Koyama,K., Makishima,K., Tanaka,Y. and Tsunemi,H. 1986, PASJ **38**, 121.

[LEA86] Leahy,D.A. et al. 1986, manuscript in preparation.

[MAK84] Makishima,K. 1984, Proc. Symposium "X-ray Astronomy '84", ed. M.Oda and R.Giacconi (June 1984, Bologna), published from ISAS, p.165.

[MAK86] Makishima,K. et al. 1986, Ap.J. submitted (ISAS RN #321).

[MAS84] Masai,K. 1984, Astrophys. Space Sci. **98**, 367.

[MAT85] Matsuoka,M. 1985, Proc. ESA Workshop on Cosmic X-ray Spectroscopy Missions (June 1985, Lyngby, Denmark), p.149.

[MAT86] Matsuoka,M., Ikegami,T. and Koyama,K. 1986, PASJ, in press (ISAS RN #309).

[MLK85] Makino,F., Leahy,D.A. and Kawai,N. 1985, Space Sci. Rev. **40**, 421.

[M&M83] Morrison,R. and McCammon,D. 1983, Ap.J. **270**, 119.

[MUR84] Murakami,T. et al. 1984, PASJ **36**, 691.

[NAG86] Nagase,F. et al. 1986, submitted to PASJ (ISAS RN #306).

[NAK86] Nakajo,M. 1986, Master Thesis, University of Kyoto.

[OHA84a] Ohashi,T. et al. 1984, PASJ **36**, 699.

[OHA84b] Ohashi,T. et al. 1984, PASJ **36**, 719.

[OKU86] Okumura,Y., Tsunemi,H., Yamashita,K. et al.1986,in preparation.

[PAR80] Parkes,G.E., Mason,K.O., Murdin,P.G. and Culhane,J.L. 1980, MNRAS **191**, 547.

[PEN86] Penston,M.V. 1986, this volume.

[R&S77] Raymond,J.C. and Smith,B.W. 1977, Ap.J. Suppl. **35**, 419.

[SAT86] Sato,N. et al. 1986, submitted to PASJ (ISAS RN #316).

[SUZ84] Suzuki,K. et al. 1984, PASJ **36**, 761.

[TAN84] Tanaka,Y. et al. 1984, PASJ **36**, 641.

[TAN86] Tanaka,Y. 1986, an invited talk presented at IAU Colloquium No.89, "Radiation Hydrodynamics in Stars and Compact Objects" (June 1985, Copenhagen : ISAS RN #303).

[TUN86] Tsunemi,H. et al. 1986, Ap.J. in press.

[WAN86] Wang,B., Inoue,H., Matsuoka,M., Tanaka,Y., Hirano,T. and Nagase,F. 1986, PASJ in press (ISAS RN #317).

[WAR85] Warwick,R.S., Turner, M.J.L., Watson,M.G. and Willingale,R. Nature **317**, 1985.

[WHI86] White,N.E., Peacock,A., Hasinger,G., Mason,K.O., Manzo,G., Taylor,B.G. and Branduardi-Raymont,G. 1986, MNRAS **218**, 129.

[W&S84] White,N.E. and Swank,J.H. 1984, Ap.J. **287**, 856.

[WSH83] White,N.E., Swank,J.H and Holt,S.S. 1983, Ap.J. **270**, 711.